SAND2019-12088J

Seismic Characterization of the Nevada National Security Site Using Joint Body Wave, Surface Wave and Gravity Inversion

Leiph Preston[1], Christian Poppeliers[1], and David J. Schodt[2]

1. Sandia National Laboratories, Albuquerque, NM

2. Sandia National Laboratories, Albuquerque, NM. Now at University of New Mexico, Albuquerque, NM.

Corresponding Author: L.A. Preston, P.O. Box 5800, MS-0750, Sandia National Laboratories, Albuquerque, NM 87185, USA (lpresto@sandia.gov)

Abstract

As part of the series of Source Physics Experiments (SPE) conducted on the Nevada National Security Site in southern Nevada, we have developed a local-to-regional scale seismic velocity model of the site and surrounding area. Accurate earth models are critical for modeling sources like the SPE to investigate the role of earth structure on the propagation and scattering of seismic waves. We combine seismic body waves, surface waves, and gravity data in a joint inversion procedure to solve for the optimal 3-D seismic compressional and shear wave velocity structures and earthquake locations subject to model smoothness constraints. Earthquakes, which are relocated as part of the inversion, provide P- and S-body wave absolute and differential travel times. Active source experiments in the region augment this dataset with P-body wave absolute times and surface wave dispersion data. Dense ground-based gravity observations and surface wave dispersion derived from ambient noise in the region fill in many areas where body-wave data are sparse. In general, the top 1-2 km of the surface is relatively poorly sampled by the body waves alone. However, the addition of gravity and surface waves to the body wave dataset greatly enhances structural resolvability in the near surface. We discuss the methodology we developed for simultaneous inversion of these disparate data types and briefly describe results of the inversion in the context of previous work in the region.

INTRODUCTION

The Source Physics Experiments (SPE) consisted of a series of buried chemical explosions conducted near the north end of Yucca Flat, Nevada National Security Site (NNSS), in southern Nevada (Snelson *et al.*, 2013). The purpose of SPE is to explore and gain a better understanding of explosion source phenomenology with particular emphasis on the generation and propagation of seismic shear waves, especially in terms of nuclear non-proliferation. The 3-D structure of the earth affects propagation of seismic waves via refraction, reflection and scattering of the generated wavefield. Therefore, to accurately simulate propagation of seismic waves, the 3-D structure of the earth must be accurately known. In pursuit of this goal, we use a joint inversion technique to estimate the regional 3-D seismic velocity structure near the SPE site. The joint inversion uses compressional (P) and shear (S) body wave travel times in combination with seismic surface wave dispersion and gravity measurements.

Using these three different types of data allows us to obtain a better resolved image of the earth structure than if only one type of data were used. This is due to the fact that these datasets complement each other; the strengths in one dataset can offset the weaknesses in another. Body waves can provide excellent resolution of earth structure in areas of ample crossing ray paths. Body wave resolution is typically best at the depths where most earthquakes occur. Near the surface, however, ray paths are nearly vertical, providing poor resolution in this region. Additionally, below the turning depths of most rays, body wave resolution is poor to non-existent. Surface waves, on the other hand, are most sensitive to earth structure at the surface of the earth. Their sensitivity as a function of depth depends on the frequency of the surface wave, with longer

66 period waves being more sensitive to deeper structure (e.g., Aki and Richards, 2002). This allows
67 surface waves to help with both the shallowest portions of the model as well as the deepest,
68 improving vertical resolution. Their weakness, however, is that they are sensitive to a relatively
69 large volume of the earth and, thus, have poorer horizontal resolution compared to body waves
70 alone. Gravity measurements depend on the distribution of mass within the earth. For a given
71 size and density contrast, a structure located deep within the Earth will produce a spatially broad,
72 low amplitude gravity signature compared to a similar structure located near the Earth's surface,
73 which will produce a relatively high amplitude, short spatial wavelength gravity signature.
74 However, since each gravity observation has sensitivity to every point in the model, a trade-off
75 exists between depth to an anomaly and the anomaly's density (e.g., Turcotte and Schubert, 1982).
76 When gravity measurements are combined with body waves and surface waves, however, this non-
77 uniqueness can be mitigated. The high wavenumber gravity information can provide excellent
78 horizontal resolution in the near surface, while longer wavenumber structure can help control
79 deeper structure, constrained by the seismic datasets.
80
81 The advantages of using multiple types of data in inversions has been recognized and used by
82 various authors for decades. The most common usage is the combination of two different types of
83 data (such as gravity and body waves) in order to remove some non-uniqueness from the solution
84 space. For example, Obrebski *et al*. (2012) utilized joint inversion of body waves and surface
85 waves in a regional tomographic image of China, and Zhang *et al.* (2014) used the same
86 combination of data for a local 3-D P- and S-wave model of the San Andreas Fault Observatory
87 (SAFOD) site. Data from gravity and body waves were jointly inverted by Roecker *et al.* (2004)
88 to obtain a structural model near the SAFOD site and by Bergman *et al.* (2012) to derive a regional

89 model in Eurasia. Julià *et al.* (2000) inverted teleseismic P-wave receiver functions and surface
90 wave phase and group speed dispersion curves for crustal and upper mantle structure for the
91 Arabian Shield. Maceira and Ammon (2009) jointly inverted surface wave and gravity data for a
92 regional model of central Asia. More recently, Syracuse *et al.* (2017) and Roecker *et al.* (2017)
93 combined body wave, gravity, and surface wave data to jointly invert for 3-D P- and S-wave
94 structural models of Utah and eastern Africa, respectively. Syracuse *et al.* (2017) utilized P- and
95 S-body wave arrival times, maps of surface wave group and phase speed derived from ambient
96 noise, and satellite-based gravity observations in their model of the crust and upper mantle under
97 Utah. Similarly, Roecker *et al.* (2017) inverted P- and S-travel times from local earthquakes jointly
98 with surface wave dispersion data from ambient noise and gravity observations for a crustal model
99 under the East African Rift.
100
101 In this paper, we first describe the datasets used in this study, then we discuss the methodology we
102 use to perform the simultaneous inversion of absolute and differential P- and S-body wave travel
103 times, surface wave dispersion curves, and ground-based gravity data. Finally, we briefly examine
104 results of the joint inversion primarily in the context of our previous P-body-wave-only inversion
105 of the region (Preston *et al.*, 2007).
106
107 **Geologic Background of the Nevada National Security Site**
108
109 The study region, including the Nevada National Security Site (NNSS), is situated within the
110 southern Walker Lane Belt (Stewart, 1988) in the broader context of the Basin and Range province.
111 Northwest striking, strike-slip faulting within the East California Shear Zone in the southwest

112 portion of the study area transitions toward roughly north-south oriented normal faulting to the
113 north and east. In addition to these broader geological contexts, the NNSS region is punctuated
114 by Miocene caldera complexes and waning post-Miocene volcanism (O'Leary *et al.,* 2002;
115 Vaniman *et al.,* 1982*;* Crowe *et al.,* 1995). The Timber Mountain, Oasis Valley, and Silent Canyon
116 caldera complexes produced voluminous tuff sequences that cover or fill much of the area's mesas
117 and basins. As is typical of the Basin and Range, many basins in the area are covered surficially
118 with Cenozoic alluvium deposits, and surficial exposures of pre-Cenozoic rocks are primarily
119 limited to mountain ranges. The NNSS proper contains pre-Cenozoic exposures in the ranges
120 surrounding Yucca Flat and in the far south in the Specter Range, and notably in the Climax (site
121 of SPE phase 1) and Gold Meadows granitic stocks (Phelps *et al.,* 2004). Most other surficial
122 deposits on the NNSS are Cenozoic tuff and alluvium deposits. The major geologic and
123 geographic features discussed herein are shown in Figure 1a.
124
125 ## DATA
126 ### Body Waves
127
128 The body wave data set contains absolute and differential travel times from earthquakes and active
129 sources. We utilize P- and S-wave travel times from earthquakes recorded on the United States
130 Geological Survey (USGS) analog seismograph network from 1981-1992, the same network
131 operated by the University of Nevada Reno (UNR) from 1992-1995, and the combined analog and
132 digital array from 1995-2014. Earthquakes recorded on the combined network (operated by the
133 UNR) provide the vast majority of body wave travel times. Nearly 66,800 earthquakes contribute
134 approximately 615,000 P-wave and 345,000 S-wave absolute travel times, with a median number

of 17 picks per earthquake. Additionally, cross-correlations of UNR earthquake catalog waveforms provides a differential arrival time data set with a total of 297,000 P- and 197,000 S-wave differential times. We did not pick any body wave travel times as part of this study. Rather, the absolute arrival times and their estimated arrival time picking errors were obtained from their respective source earthquake catalogs, which were picked and verified by various analysts. No automatic (computer) picks are included. Starting earthquake locations are based on global relocations (not perturbations) of the events within the starting 3-D model. Differential times were derived by cross-correlating selected earthquake waveforms recorded at common stations, keeping only differential times from pairs of events with correlation coefficients greater than 0.7 (Preston and von Seggern, 2007; Waldhauser and Ellsworth, 2000). Figure 1b shows the distribution of earthquakes used in this study as black dots.

In addition to body waves derived from earthquakes, absolute P-wave arrival times from active sources are also included in the data set. These consist of arrival times from 90 underground nuclear explosions (S. Harmson, personal communication, 1993), a series of USGS experiments focused on Yucca Mountain from 1983-1985 (Hoffman and Mooney, 1984; T. Brocher, personal communication, 2005), the 1993 Non-Proliferation Experiment (Smith *et al.*, 2000; Denny, 1994), the Watusi experiments (Bhattacharyya *et al.*, 2003), the SPE Large-N array (Mellors *et al.*, 2018), the THOR1 and THOR2 experiments (Toney *et al.*, 2019), and the SPE experiments. The locations and times of the underground nuclear experiments were corrected using the information from Springer *et al.* (2002). However, due to large misfits of the underground experiment data compared to other data, the origin times of the nuclear experiments are not fixed but are allowed to float during inversion. The active source data are shown in Figure 1b as red squares.

158

159 The body wave data (both active and earthquake) were recorded on a total of 526 unique seismic
160 stations. Some of the stations were only temporarily used for specific experiments, while others
161 recorded events for several years. Seismic stations used in the study are shown as green triangles
162 in Figure 1b. In total, there are 1,577,727 body wave travel times, absolute and differential, of
163 which about 541,000 are S-wave picks. In relation to the data set used in Preston *et al.* (2007),
164 which only utilized absolute P body wave travel times, this new work includes all picks from the
165 older study plus S wave picks from earthquakes included in that study and new earthquakes and
166 active source data that were not available at the time.

167

168 **Surface Waves**

169

170 We use surface wave data that were derived from cross-correlations of ambient noise at select
171 stations in the UNR and SPE seismic networks, from surface waves observed as part of the THOR1
172 and THOR2 active source experiments in Yucca Flat (Toney *et al.*, 2019), and from active source
173 interferometry of SPE-5 observed on the SPE Large-N array (see Mellors *et al.*, 2018 for
174 information on the Large-N deployment). For the ambient noise study, 51 station pairs are used,
175 with 36 pairs from the UNR network and 15 pairs from the SPE backbone network (Figure 2). We
176 used the MSNoise software package (Lecocq *et al.*, 2014) to process the ambient noise data set to
177 produce empirical Green's functions for each station pair. To estimate the Green's functions
178 needed for the dispersion analysis, we stacked one year of ambient seismic noise, processed in one
179 day increments. Additionally, we used 382 station pairs from the SPE-5 Large-N array to produce
180 vertical-component empirical Green's functions using source interferometry (e.g., Halliday and

181 Curtis, 2008; Wapenaar *et al.*, 2010). Specifically, we found four linear sub-arrays of the Large-
182 N that were co-linear with the SPE-5 source location and cross correlated the demeaned and
183 filtered (1-5 Hz) vertical component seismogram with all the other seismograms in each linear
184 sub-array, producing a total of 11,193 surface wave dispersion picks.
185
186 To estimate the dispersion relationships for the station pairs in the UNR network, we used the
187 single station multiwavelet algorithm introduced in Poppeliers and Preston (2019). The primary
188 advantage of this method is that it provides error estimates along with group- and phase-speeds
189 using only a single time series. A second advantage is that the decomposition can be tuned to
190 produce stable, higher resolution results over a desired passband, or to emphasize certain pass
191 bands over others (see Figure 4 of Poppeliers and Preston, 2019). The multiwavelets, when applied
192 as the multiwavelet transform, act as a series of mutually orthogonal filter banks. Hence the
193 method decomposes the cross correlograms into several suites of narrow band realizations, from
194 which we obtain multiple dispersion estimates. Standard statistical methods can then be used to
195 produce a mean dispersion curve and its uncertainty for each station pair. By knowing the
196 separation for each station pair, we can transform the dispersion curve into a group velocity. For
197 our analysis, we used ten wavelet pairs to compute ten dispersion estimates for each station pair.
198 We then computed the mean and standard deviation for each station pair which was then used in
199 the inversion (Figure 3). To obtain phase velocity, we use the phase-matched filter method
200 introduced by Herrin and Goforth (1977) as implemented in Poppeliers and Preston (2019). If the
201 phase matched filter accurately represents the surface wave dispersion along the path between the
202 stations, then cross correlating the phase matched filter with the original correlogram should result
203 in a symmetric, band limited pulse centered at zero lag for all frequencies (Figure 3d).

Only group speeds were found for the SPE stations. The above described method of phase and group speed determination proved to be too unstable for the SPE stations, primarily because of a strong long period wave at near-zero lag time interfering with the surface wave. This near-zero lag time wave could be the body wave arrivals on the Green's Function. Thus, in order to compute the group speeds for the SPE station pairs, the cross-correlograms were narrow band-pass filtered and the peaks of the envelope functions of the resultants were picked manually.

In total, 237 phase and nearly 92,000 group speed measurements were collected. The UNR station pairs allowed phase and group speeds to be determined from 2 to 10 s period. The SPE backbone station pairs, due to their shorter offsets, allowed determination from about 1 to 5 s period. Due to the close station spacing and very short offsets for the SPE Large-N array, we obtained surface wave dispersion estimates from 4-30 Hz for stations in this array.

Gravity

We obtained the gravity data from the University of Texas El Paso's (UTEP) gravity and magnetic national data repository (Hildenbrand *et al*., 2002). Approximately 25,000 individual gravity measurements, collected on-site, were obtained for the data region (Figure 4). The density of measurements varies greatly throughout the study area with the central portions of the model tending to have the highest concentration. For the inversion, we used the complete Bouguer anomalies as provided in the UTEP dataset.

METHOD

Due to the different physics embodied in seismic body-waves, seismic surface-waves and the gravity field, we require different implementations for the forward and inverse problems for each data type. The theory behind body wave tomography, surface waves, and gravity are provided in many texts (e.g., Aki and Richards, 2002; Shapiro *et al*., 2005; Turcotte and Schubert, 1982). These diverse datasets are combined in a nonlinear, iterative inversion technique that simultaneously solves for optimal earthquake hypocentral locations and P- and S-wave three-dimensional velocity structure subject to model smoothness constraints (see Regularization section). P- and S-body waves utilize 3-D ray-tracing and travel time calculations via the Vidale-Hole algorithm (Vidale, 1990; Hole and Zelt, 1995). The specifics of the P-wave tomography implementation are described in Preston (2003). We perform the S-wave tomography in precisely same manner as the P-wave tomography, but we use a separate 3-D S-wave grid to trace S-wave arrivals. Rather than solve for P- and S-velocities directly, we solve for P-wave slowness (1/Vp), since the P-wave travel time is linearly related to the wave slownesses along a ray path, and the Vp/Vs ratio. The Vp/Vs ratio allows us to place permissibility constraints on S-wave velocities in areas well sampled by P-waves but poorly sampled by S-waves in our bound least squares algorithm (see Regularization section). The following sections describe the implementation of Vp/Vs, surface waves and gravity in the algorithm.

Vp/Vs

The forward problem predicts the seismic travel time for a given model. The S-wave velocities are computed from the current Vp model and Vp/Vs model, i.e.,

$$s_S = s_P R_{PS}$$

with s_S the S-slowness, s_P the P-slowness and R_{PS} the Vp/Vs ratio; thus, the S-wave travel time is

$$t_s = \sum S_s l$$

summed along the S-wave ray path, with each segment of length l.

The inverse problem is the sensitivity of the travel time to perturbations in the Vp/Vs ratio. This sensitivity can be derived from the above two equations, so

$$\delta t_S = \sum (R_{PS}\delta S_P + S_P \delta R_{PS}) l$$

268 with the linearizing assumption that the ray path remains fixed. Since the ray path does depend on
269 the distribution of velocities, i.e., this is a non-linear problem, the inversion procedure is iterated
270 until changes in the model are small.
271
272 **Surface Waves**
273
274 Unlike body waves, which we approximate as a ray path, we approximate the surface waves as
275 affecting, and being affected by, a volume of the earth. Because of the computational expense of
276 computing full 3-D surface wave phase and group velocities and sensitivity kernels, we use an
277 approximation in order to compute these quantities rapidly, while still allowing reasonable
278 accuracy. Specifically, we use separate Vp and Vs model grids for surface wave inversions that
279 are tied via constraint equations to the primary body wave Vp and Vs grids (Figure 5). The surface
280 wave grids have a node density that is inversely proportional to depth: the highest node density
281 exists at the surface and becomes coarser with depth. The surface layer, which follows topography,
282 matches the resolution of the underlying body wave grid. Three nodes below the lowest
283 topography in the model, the surface wave grid coarsens by doubling the node spacing in all three
284 dimensions. This node spacing is retained for three grid nodes in depth before another doubling
285 in the node spacing occurs. This process continues until the maximum depth of the model domain.
286 The surface wave P and S slownesses associated with a given grid node are simply the mean
287 slownesses of the body wave nodes contained within that surface wave cell; this mean value
288 constraint is enforced during the matrix inversion step so that the surface and body wave grids
289 never differ by more than 1 m/s. These 3-D Vp and Vs models are converted to 1-D average
290 models individually for each source-receiver pair using the surface wave sensitivity volume, which

is a function of period (Lin and Ritzwoller, 2010). These sensitivity kernels are truncated at the first zero crossing, giving an approximately oval shape at the surface; thus, the sensitivity outside this oval is zero and inside it is normalized so that the sum over the area is unity within each 1-D layer.

Using this series of 1-D layers, the surface wave phase and group speeds at different frequencies are computed using a finite element Rayleigh solver (e.g., Lysmer*, 1970*). The sensitivity of changes in phase and group speeds to changes in the 1-D Vp and Vs layers are computed using finite differences by perturbing each layer's Vp and Vs individually. We then distribute these 1-D sensitivities to the 3-D surface wave grid nodes contained in each layer based on the areal sensitivity kernels described above. This approximates the 3-D sensitivity of changes in the phase or group speed to changes in the 3-D Vp and Vs models.

Gravity

Each gravity measurement is dependent on every point in the model; therefore, we use a separate grid for the prediction and inversion of the gravity data. Also, because gravity varies with the inverse of distance squared, deeper structures are smoothed, allowing the separate gravity grid to coarsen with depth (Figure 5). As with the surface wave grid, the value of the P-slowness for each gravity cell is the mean value of the body wave nodes contained within each gravity cell. Extra constraint equations additionally ensure that the two grids never differ by more than 1 m/s during the inversion process. This greatly reduces required computational memory and effort, while still honoring the strengths of the gravity dataset.

In order to predict and find gravity sensitivities to changes in the 3-D P-wave velocities, we must assume a relationship between density and Vp. For our work here, we use 30% of the density computed from Eq. 1 of Brocher (2005) plus 70% of the density from Gardner's relation (Gardner et al., 1974). This admixture gives reasonable values of densities for the full range of P-wave velocities encountered in the model. The derivative of this relation with respect to changes in P-wave velocity provides the necessary sensitivities for inversion. We assume that the direct effects of S-waves on density (and vice versa) are zero.

The predicted value of gravity at any point on the surface depends upon all of the density values in the earth. However, since we are not modeling the entire earth we need to account for effects outside the model domain. This is achieved in two ways: first, we use extra buffer zones in the horizontal dimensions to mitigate against edge effects in the X and Y directions. These buffer zones assume linearly decreasing density anomalies outside the model domain. Secondly, we also invert for a constant gravity value, common to all observation points. This is equivalent to finding the best-fit infinite slab of a given thickness and density perturbation lying somewhere under the model domain and can be thought of as removal of the mean gravity anomaly.

Regularization

Regularization is the method by which the system of equations is made solvable with standard matrix inversion techniques. The system of equations as defined by the above data types is over-determined in certain areas where much of the data overlap and under-determined in other areas

where data are sparse. The model matrix, defined by the sensitivity to changes in the model parameters described above, is augmented by further equations that regularize the matrix. For our work here, we employ differing methods of regularization for each of the data types used in the inversion.

The body P-wave and Vp/Vs grids are regularized by applying an anisotropic smoothness constraint. We use the second order accurate finite difference 3-D Laplacian function but allow sharper gradients in the depth dimension compared to the horizontal dimensions. This allows resolution of the high vertical velocity gradients typically found in the shallowest depths of the crust. Even with this anisotropic Laplacian smoothing we are still capable of imaging strong horizontal gradients that could be associated with faults. Furthermore, since model resolution is expected to decrease once below the seismogenic depth, we force the model to be smoother below 15 km depth. We apply a final regularization layer by smoothing areas more where data density is low compared to where data density is high. These regularizations both impose realistic physical constraints and control the effect of outliers.

We admit that regularization is a somewhat subjective process. The smoothness or roughness of the resulting model is subject to the researcher's biases, assumptions, and preconceptions. For this model, our basic assumption is that a smooth model is preferable to a rougher model which equally fits the data. We tested many different combinations of smoothing parameters for Vp, Vp/Vs, depth smoothing, and data density smoothing. We desired a model that would be rough enough at the surface to honor the density of active sources and gravity observations and yet not over-fit data at depth. We found that a smoother model at depth could fit the data equally well as a rougher

360 model; thus, our bias is towards the smoother model. Obviously, this choice eliminates the
361 possibility of imaging very small structures at depth, but it also prevents small, likely fictitious
362 features (e.g., numerical artifacts) from being interpreted as actual Earth structure.
363
364 We also place constraints on the range of values permissible for Vp and Vp/Vs. These are imposed
365 directly within the matrix inversion step so that a fully self-consistent solution is computed
366 (Bierlaire *et al.*, 1991). These constraints ensure that Vp, and most importantly Vp/Vs, are
367 physically realistic. For example, in areas with many active sources, the Vp model is well
368 constrained at shallow depths, showing lower P-wave velocities there. However, with no
369 comparable S-wave control, S-wave velocities at depth would get smoothed upwards toward the
370 surface. This could cause the shallow S-wave velocity to be larger than is physically possible
371 compared to the P-wave speeds. By constraining the Vp/Vs ratio to physically realistic limits, this
372 problem can be avoided.
373
374
375 **Assembly of the Joint Inversion**
376
377 We perform a classical linearized least squares inversion, solving the general set of linear equations
378 of the form
379
380 $\mathbf{Ax} = \mathbf{b}$, (1)
381

where the matrix **A** contains the sensitivities of changes in the observations to changes in medium parameters augmented by regularization and constraint equations, the vector **x** contains perturbations to the model parameters (body wave P- and S-slownesses, earthquake hypocentral parameters, surface wave grid P- and S-wave slownesses, and gravity grid P-wave slownesses), and the vector **b** contains observed residuals augmented by regularization and constraint residuals. Specifically, Equation 1 takes the form:

$$\begin{bmatrix} P_{body} & S_{body} & E_{hypo} & 0 & 0 & 0 \\ 0 & 0 & 0 & P_{surf} & S_{surf} & 0 \\ 0 & 0 & 0 & 0 & 0 & P_{grav} \\ L_P & 0 & 0 & 0 & 0 & 0 \\ 0 & L_S & 0 & 0 & 0 & 0 \\ 0 & 0 & L_{hypo} & 0 & 0 & 0 \\ K_{Pb} & 0 & 0 & K_{Ps} & 0 & 0 \\ 0 & K_{Sb} & 0 & 0 & K_{Ss} & 0 \\ G_{Pb} & 0 & 0 & 0 & 0 & G_{Pg} \end{bmatrix} \begin{pmatrix} \partial P_{body} \\ \partial S_{body} \\ \partial E_{hypo} \\ \partial P_{surf} \\ \partial S_{surf} \\ \partial P_{grav} \end{pmatrix} = \begin{bmatrix} r_{body} \\ r_{surf} \\ r_{grav} \\ -L_P m^{(i)} \\ -L_S m^{(i)} \\ 0 \\ 0 \\ 0 \\ 0 \end{bmatrix} \quad (389)$$

where P_{body} are the sensitivities of changes in travel times to changes in P-body wave slownesses, S_{body} are the Vp/Vs-body wave sensitivities, E_{hypo} are sensitivities to changes in earthquake hypocentral parameters and explosion experiment origin times (i.e., travel time gradients evaluated at the current iteration's locations), P_{surf} are sensitivities of changes in group or phase speed to changes in surface wave P slownesses, S_{surf} are the Vp/Vs-surface wave sensitivities, P_{grav} are the sensitivities in changes of gravity to changes in the gravity grid slownesses (via the Vp-gravity relation described above), L_P forms the P-body wave slowness regularization matrix of the anisotropic 3-D Laplacian, L_S forms the Vp/Vs body wave regularization matrix, L_{hypo} is the hypocentral regularization matrix (a scaled identity matrix to favor small perturbations), K_{Pb} and K_{Ps} forms the linkage between the P body wave and surface wave grids, K_{Sb} and K_{Ss} forms the

linkage between the Vp/Vs body wave and surface wave grids, and G_{Pb} and G_{Pg} forms the linkage between the P body wave and gravity grids. The column vector on the left side of the equation explicitly shows the unknowns we are solving for: perturbations in the P body wave slownesses, Vp/Vs body wave values, hypocentral parameters, P surface wave slownesses, Vp/Vs surface wave ratios, and P gravity grid slownesses, from top to bottom. The right hand side of the equation contains the body wave travel time residuals, r_b, surface wave group and phase speed residuals, r_s, gravity residuals, r_g, and regularization residuals, which, since we are aiming for a smooth total model, not just in perturbation, is equal to the negative of the roughness of the present model, $m^{(i)}$. We desire the current iteration's perturbations in hypocentral parameters be small; thus, the hypocentral regularization term is equal to zero. Since the linkage equations enforce the mean of the body wave slownesses within a surface wave or gravity cell be equal to the value of that surface or gravity cell, there is no residual on the right-hand side for these terms. Data are weighted by the inverse of each observation's estimated uncertainty, and each regularization matrix contains a scalar parameter that can be used to adjust each regularization term's weight in the overall inversion.

Model Parameters

The spatial extent of the model is defined by -117.33° to -115.43° longitude, +36° to +38° latitude, (about 220 km N-S by 160 km E-W) and from the topographic surface to ~40 km depth. Model node spacing is set at 2 km by 2 km horizontally and 1 km vertically. The starting model consisted of the model presented in Preston *et al*. (2007) expanded by smooth extrapolation outside that

model's domain. Note that the depths discussed below are relative to sea level, with the mean topographic surface about 1.5 km above sea level (depth of -1.5 km). The lowest elevations in the model are just below sea level in Death Valley, in the southwest portion of the model domain. Elevations generally increase south to north in the model region, with the southern Amargosa Desert having an elevation of ~250 m in the south increasing to over 2000 m (-2 km depth) for Pahute Mesa in the north. The final weighted root mean square (RMS) residuals and variance reductions of the various data types are provided in Table 1.

RESULTS

The addition of multiple data types increases the resolution of the estimated seismic velocity structure relative to body-wave-only images. For example, Figure 6a shows the estimated Vp obtained by inverting only seismic body waves, and Figure 6b shows the Vp model obtained by inverting the joint data set. Note that in this figure, the displayed Vp is a constant-depth (0 km, i.e. sea level) slice through the model. When using the joint data set, the basins and ranges in the north portion of the model are well defined with high velocity ranges and lower velocity basins. Conversely, when using only the body wave data, there is no clear Vp structure in this region: velocities vary smoothly, being nearly constant in the northern portion of the model. Earthquakes (black dots in the figures are events within 1 km of sea level) also relocate differently between the two models due to these changes in structure (the earthquakes in common between the two data sets average ~400 m shallower in the new model). The effects of surface waves are apparent by comparing the checkerboard test cross-sections in Figure 7, which shows the Vs checkerboard results at 37.2°N latitude where only P- and S-body waves and gravity data are included (Figure

447 7a) versus the same results when surface waves are added (Figure 7b). As noted above, gravity
448 data is assumed to contribute nothing to the S-wave structure except through the Vp/Vs constraints,
449 and the S-body-waves come solely from earthquakes. The addition of surface waves enhances
450 resolution at the very shallowest depths (<0 km depth), on the east and west edges of the model,
451 and in the deeper portions of the model. Thus, the surface waves contribute to S-model resolution
452 via both their stronger depth sensitivity in the central portion of the model and their different
453 horizontal spatial coverage relative to earthquake S-body wave ray paths.
454
455 The P-wave velocities from the surface down to a depth of at least 4 km (Figure 8a-d, S1-S4)
456 closely mimic topographic features. In general, the large-wavelength P-wave velocity features
457 mimic the topography at greater depths but tend to be smoother than the P-wave structures at
458 shallow depths (Figures 8e,f, S5-S6). Low velocity sediments and alluvium can be many
459 kilometers thick within basins while ranges generally consist of stronger materials with faster
460 seismic velocities. Below maximum basin depths, lower than average seismic velocities could be
461 associated with weaker, fractured zones (Catchings, 1992) or by changes in rock type. The
462 estimated P-wave velocities of the Death Valley region also tend to mimic the topography, with
463 high velocity ranges and low velocity basins, which persists to about 10 km depth (Figure 8e, S5).
464 For depths greater than 10 km, the P-wave velocity blends into a larger region of generally elevated
465 velocities (>6.45 km/s) lying to the south at depths of approximately 15 km (Figure 8f, S6). Also
466 at these depth, a north to south general increase in P-wave velocities is apparent (Figures 8e and
467 8f, S5-S6). This pattern mimics the north to south increase in the complete Bouguer anomaly
468 (Figure 4), which has been interpreted by Saltus and Thompson (1995) as being due to differences
469 in the properties and thickness of the crust and to more buoyant asthenosphere to the north. In

order to test how much of the deep north-south seismic velocity gradient is possibly due to this gravity gradient, we compared the joint modeling results with results from body-wave-only results. We find that the same general north-south velocity gradient is present in the body-wave-only model, making us conclude that the deep velocity gradients in the joint model are not solely an artifact of the gravity data.

We estimate higher P-wave velocities under the Eleana Range, which persist from near the surface down to about 15 km depth. Lower than average seismic velocities are coincident with the eastern end of the Rock Valley Fault Zone, located on the eastern edge of the NNSS, that extend from the surface to ~15 km depth. The estimated P-wave velocity at the surface (-1 km depth) of Yucca Flat, located on the eastern edge of the NNSS are lower in the eastern portion compared to the western boundary (Figure 9), with the break roughly coincident with the Carpetbag Fault, consistent with Phelps *et al*. (1999). The estimated P-wave velocities of the ranges surrounding Yucca Flat are higher than average, which is common of the ranges in this region. In general, the P- and S-wave velocities that we estimated using our joint inversion are higher than other Yucca Flat models (e.g., Schramm *et al*., 2012) at the shallowest depths, which may be due to a bias introduced by the Vp-density relation we assumed. Higher Vp velocities at depths greater than 1 km (~2 km below the surface) suggest a maximum depth of Yucca Flat consistent with Phelps *et al.* (1999). As the depth increases beyond 2 km, seismic velocities beneath Yucca Flat actually decrease relative to those above it, nearly merging with a larger low velocity anomaly that extends southward to the Rock Valley Low Velocity Zone. However, resolution analysis suggests that under Yucca Flat at this depth, structures on the scale of this feature would be marginally resolved, so the low estimated Vp velocity structure at this depth may be an artifact smeared northward from

493 eastern Rock Valley region, where it is resolvable. At 10 km depth Yucca Flat consists of higher
494 velocities in the north, with features merging with the larger high velocity structure to its west,
495 under Syncline Ridge, and lower velocities in the south, but is generally seismically fast overall,
496 probably due to smearing from the high velocity area to its west. Timber Mountain, located in the
497 central portion of the NNSS, is imaged as a relatively high velocity island encircled by lower
498 velocities at the surface. Low velocities lie immediately north under the Silent Canyon Caldera,
499 Pahute and Rainier Mesas, for the entire depth range of the model.
500
501 In cross-section (Figure 9) basins and ranges are clearly seen. A broad higher Vp region
502 approaches the surface under the Bullfrog Hills. The expression of Timber Mountain can be seen
503 in this image as a relatively narrow, high velocity region with lower velocities to each side (Oasis
504 Valley and Buckboard Mesa). The shallow portion of Yucca Flat is also imaged with a shallower
505 western and deeper eastern portion as mentioned above.
506
507 P-wave velocity structures imaged here bear a close correspondence to structures seen in the well-
508 resolved portions of the P-wave velocity model presented in Preston *et al.* (2007), especially above
509 5 km depth. The primary differences at shallow depth are due to the higher resolution available
510 by using the joint data set. Basins such as Crater Flat, Amargosa Basin, Jackass Flat and Yucca
511 Flat are better resolved in higher resolution compared to the older study. Not only are mountain
512 ranges on the peripheries of the old model (e.g., the Funeral Mountains) better resolved in the new
513 model but also those near the central portion of the model, such as Timber Mountain. However,
514 below about 5 km depth, even in areas with high data coverage in the older model, differences do
515 emerge generally on the smaller scale. For example, Preston *et al.* (2007) discusses a low velocity

516 zone under NE Jackass Flat at 5 km depth. This structure is still resolved using the joint data set
517 but is much more subtle. Regardless, larger scale structures have a good correspondence between
518 the two models even at these depths. Low seismic velocities are imaged under the Silent Canyon
519 Caldera complex region and higher seismic velocities are centered under Syncline Ridge. These
520 differences in images at depth can be largely attributed to the much smoother model being sought
521 in the current study. Although the RMS P-wave travel time misfits between the two models are
522 virtually identical, we are able to achieve this with a smoother model at depth using our joint
523 inversion. Despite these differences, none of the basic conclusions of Preston *et al*. (2007) are
524 contradicted by these new results.
525
526 The S-wave velocity structure roughly follows the same trends as the P-wave structure; however,
527 Vp/Vs images are smoother primarily due to volume averaging effects. High Vp/Vs ratios (>1.8)
528 near the surface occur over an area that stretches from the Silent Canyon Caldera complex in the
529 north to just east of Death Valley in the south (Figure 10a, S7). This north-south trend is
530 interrupted by an ENE trending low Vp/Vs (<1.67) structure that roughly follows seismicity within
531 the Rock Valley Fault zone into the Little Skull Mountain region between sea level and ~4 km
532 depth (Figures 10a-d, S7-S10). For depths of 8 km and more, we observe broad areas of somewhat
533 elevated Vp/Vs ratios (>1.74) south and west of Timber Mountain to Death Valley, roughly
534 coincident with the southern half of Kawich-Greenwater rift proposed by Carr (1990) (Figures
535 10e,f, S11-S12). At the shallowest depths (< 1km), Vp within the proposed rift structure generally
536 tends to be slower than average, but we see no Vp structural correlation at deeper depths. This
537 high Vp/Vs region is abruptly truncated at the northern portions of Bare Mountain and Yucca
538 Mountain, where farther north, lower Vp/Vs values associated with the Timber Mountain Caldera

539 are present. Lower than average Vp/Vs ratios lie under Yucca Flat and in a north-south line south
540 of Shoshone Peak through the main sequence of Little Skull Mountain aftershocks (Figures 10e,
541 f, S11-S12). Vp/Vs is at or below average under Pahute Mesa and Timber Mountain Caldera from
542 the surface through the deepest resolved portions of the model.
543
544 Model resolution, as depicted in the checkerboard tests (with errors distributed the same as the real
545 data), shows excellent definition of the P-wave structure within the central portion of the model
546 down to at least 4 km depth below sea level. Error analysis demonstrates that, with data errors,
547 adjacent structures with Vp contrasts of about 10-15% or less are resolvable at all scales evaluated.
548 Good to excellent recovery of 6 by 6 km horizontal blocks with 15% velocity perturbation is
549 observed down to about 4 km depth generally within NNSS proper, with rapidly decreasing
550 resolution at this scale at greater depths (Figure 11a). At the 10 by 10 km scale with 10%
551 perturbations, excellent resolution covers a broader region and persists to ~6 km depth, but
552 resolution degrades at greater depths (Figure 11b, c). At the 20 by 20 km scale, however, there is
553 near perfect recovery throughout the model area down to about 4 km depth, below which,
554 resolution begins to decrease except under NNSS proper where reasonable resolution remains until
555 ~10 km depth (Figure 11d, e). A similar pattern is observed for the 40 by 40 km block sizes at
556 10% perturbation but with overall stronger checkerboard pattern return relative to the 20 by 20 km
557 block size (Figure 11f). The strong decrease in resolvability below about 10 km depth is due to
558 the effects of a strong drop-off in body ray density at this depth coupled with the choice of greater
559 smoothing below 15 km. The increased smoothing with depth can clearly be seen on the cross-
560 section plots as well. S-wave resolution is roughly similar to the P-wave resolution, except that
561 the minimum resolvable scale is 10 km horizontally and the horizontal coverage of high resolution

562 is somewhat more restricted compared to P-waves (Figure 12). However, due to the presence of
563 surface wave data, S-waves have better resolvability at depths greater than ~5 km.
564
565 **DISCUSSION AND CONCLUSIONS**
566
567 We have jointly inverted P- and S-body wave travel times, surface wave dispersion, and gravity
568 data and derived an image of the 3-D P- and S-wave velocity structure in southern Nevada,
569 including the NNSS. The joint inversion demonstrates greater fidelity and resolution compared
570 to a model based on body waves alone. The increased resolution of the seismic velocity model
571 was the primary goal of this paper, as this model will be used to simulate the propagation of
572 seismic wavefields in this region. Specific tectonic interpretations are outside the scope of this
573 paper.
574
575 High velocity mountain ranges and low velocity basins are clearly imaged over a majority of the
576 model region using the combined dataset whereas only gross features in the central portion of the
577 model are resolved when only using seismic body waves. Although P-wave resolution is greatly
578 enhanced by the addition of gravity data, the S-wave resolution is more subtly affected by the
579 addition of surface waves in this study, most likely due to the greater volume averaging effects
580 of surface waves. However, despite this limitation, the addition of surface wave information
581 allowed greater resolvability of the shallower and deeper portions of the S-wave model and to a
582 greater lateral extent compared to the body-wave-only model. This study demonstrates the
583 improvements to geophysical modeling that can be achieved by merging disparate datasets,

where the strengths of one data type can offset weaknesses in another, providing greater fidelity and resolution of these models.

DATA AND RESOURCES

The SPE data used in this paper is available from the IRIS data center (www.iris.edu) under the name "Source Physics Experiment" (last accessed June 2019). Earthquake and surface wave data were obtained from the University of Nevada Reno Seismology Laboratory. David von Seggern (UNR) provided the cross-correlation differential body wave travel times. Rob Abbott (Sandia National Laboratories) provided the body and surface wave data from the THOR experiments. Ting Chen (Los Alamos National Laboratory) provided the Large-N P-wave arrival times. Tom Brocher (USGS) provided the USGS Yucca Mountain active source data. The gravity dataset was downloaded from http://research.utep.edu/Default.aspx?tabid=37229 (last accessed April 2019). The Supplemental Online Material includes expanded images of the panels in Figures 8 and 10.

ACKNOWLEDGEMENTS

The Source Physics Experiments (SPE) would not have been possible without the support of many people from several organizations. The authors wish to express their gratitude to the National Nuclear Security Administration, Defense Nuclear Nonproliferation Research and Development (DNN R&D), and the SPE working group, a multi-institutional and interdisciplinary group of scientists and engineers. The authors wish to thank Chrysm Watson-Ross for installation and processing for the MSNoise software. Sandia National Laboratories is a multimission laboratory managed and operated by National Technology & Engineering Solutions of Sandia, LLC, a wholly

owned subsidiary of Honeywell International Inc., for the U.S. Department of Energy's National Nuclear Security Administration under contract DE-NA0003525. This paper describes objective technical results and analysis. Any subjective views or opinions that might be expressed in the paper do not necessarily represent the views of the U.S. Department of Energy or the United States Government.

REFERENCES

Aki, K. and P.G. Richards (2002). *Quantitative Seismology*, University of Science Books, Sausalito, CA.

Bhattacharyya, J., H.E. Bass, D.P. Drob, R.W. Whitaker, D.O. Revelle, and T.D. Sandoval (2002). Description and analysis of infrasound and seismic signals recorded from the Watusi explosive experiment, September 28, 2002, in *Proceedings of the 25th Seismic Research Review - Nuclear Explosion Monitoring: Building the Knowledge Base*, Tucson, Arizona, LA-UR-03-6029: Vol. 2, pp. 587-596.

Bergman, E.A., C.A. Rowe, and M. Maceira (2012). *Crust and upper mantle structure from joint inversion of body wave and gravity data (Postprint), Annual Report 1*, Air Force Res. Lab., Kirtland Air Force Base, NM, AFRL-RV-PS-TP-2012-0038.

Bierlaire, M., Ph.L. Toint, and D. Tuyttens (1991). On iterative algorithms for linear least squares problems with bound constraints, *Lin. Alg. and its Appl.* **143**, 111-143.

Brocher, T.M. (2005). Empirical relations between elastic wavespeeds and density in the earth's crust, *Bull. Seis. Soc. Am.* **95,** no. 6, 2081-2092, doi: 10.1785/0120050077.

Carr, W. J. (1990). Styles of extension in the Nevada Test Site region, southern Walker Lane Belt: An integration of volcano-tectonic and detachment fault models, in *Basin and Range Extensional Tectonics Near the Latitude of Las Vegas, Nevada*, edited by B. P. Wernicke, *Mem. Geol. Soc. Am.*, 176, 283–303.

Catchings, R.D. (1992). A relation among geology, tectonics, and velocity structure, western to central Nevada Basin and Range, *Geol. Soc. Am. Bull.* **104**, no. 9, 1178-1192.

635 Crowe, B., F. Perry, J. Geissman, L. McFadden, S. Wells, M. Murrell, J. Poths, G. A. Valentine,
636 L. Bowker, and K. Finnegan (1995). *Status of volcanism studies for the Yucca Mountain site*
637 *characterization project*, Los Alamos Rep. LA-12908-MS, Los Alamos Natl. Lab., Los
638 Alamos, N. M.
639 Denny, M.D. (Editor) (1994). *Proc. of the Symposium on the Non-Proliferation Experiment*
640 *(NPE): Results and Implications for the Test Ban Treaties*, 19-21 April 1994, Rockville,
641 Maryland, CONF 9404100, Lawrence Livermore National Laboratory.
642 Gardner, G.H.F., L.W. Gardner, and A.R. Gregory. Formation velocity and density—the
643 diagnostic basics for stratigraphic traps (1974), *Geophysics* **39**, 770–780.
644 Halliday, D., and A. Curtis (2008). Seismic interferometry, surface waves and source
645 distribution, *Geophys. J. Int*. **175**, no. 3, 1067-1087.
646 Herrin, E., and T. Goforth (1977). Phase-matched filters: application to the study of Rayleigh
647 waves, *Bull. Seis. Soc. Am.* **67**, no. 5, 1259-1275.
648 Hildenbrand, T.G., A. Briesacher, G. Flanagan, W.J. Hinze, A.M. Hittleman, G.R. Keller, R.P.
649 Kucks, D. Plouff, W. Roest, J. Seeley, D.A. Smith, and M. Webring (2002). *Rational and*
650 *operational plan to upgrade the U.S. gravity database*, *U.S. Geol. Surv. Open File Rep. 02-*
651 *463*.
652 Hoffman, L.R. and W.D. Mooney (1984). *A seismic study of Yucca Mountain and vicinity,*
653 *southern Nevada*, *U.S. Geol. Surv. Open File Rep. 83-588*.
654 Hole, J. and B. Zelt (1995). 3-D finite-difference relfection traveltimes, *Geophys. J. Int. 121,* no.
655 2, 427-434.
656 Julià, J., C.J. Ammon, R.B. Herrmann, and A.M. Correig (2000), Joint inversion of receiver
657 function and surface wave dispersion observations, *Geophys. J. Int*. **143**, 99-112.

Lecocq, T., C. Caudron, and F. Brenguier (2014). MSNoise, a Python Package for Monitoring Seismic Velocity Changes Using ambient seismic noise, *Seis, Res. Lett.* **85**, no. 3, 715-726, 10.1785/0220130073.

Lin, F-C. and M.H. Ritzwoller (2010). Empirically determined finite frequency sensitivity kernels for surface waves, *Geophys. J. Int.*, doi: 10.1111/j.1365-246X.2010.04643.x.

Lysmer, J. (1970). Lumped mass method for Rayleigh waves: *Bull. Seis. Soc. Am.* **60**, 89–104.

Maceira, M., and C.J. Ammon (2009). Joint inversion of surface wave velocity and gravity observations and its application to central Asian basins shear velocity structure, *J. Geophys. Res*. **114**, B02314, doi: 10.1029/2007JB005157.

Mellors, R.J., A. Pitarka, E. Matzel, S. Magana-Zook, D. Knapp, W.R. Walter, T. Chen, C.M. Snelson, and R.E. Abbott (2018). The Source Physics Experiments Large N Array, *Seis. Res. Lett.* **89**, no. 5, 1618-1628, 10.1785/0220180072.

Obrebski, M., R.M. Allen, F. Zhang, J. Pan, Q. Wu, and S.-H. Hung (2012). Shear wave tomography of China using joint inversion of body and surface wave constraints, *J. Geophys. Res*. **117**, B01311, doi:10.1029/2011JB008349.

O'Leary, D. W., E. A. Mankinen, R. J. Blakely, V. E. Langenheim, and D. A. Ponce (2002). *Aeromagnetic expressions of buried basaltic volcanoes near Yucca Mountain*, Nevada, U.S. Geol. Surv. Open File, 02 – 020.

Phelps, G.A., R.C. Jachens, B.C. Moring, and C.W. Roberts (2004). *Modeling of the Climax Stock and related plutons based on the inversion of magnetic data*, Southwest Nevada, U.S. Geol. Surv. Open-File Report 2004-1345.

679 Phelps, G., V. Langenheim, and R. Jachens (1999). *Thickness of Cenozoic deposits of Yucca Flat*
680 *inferred from gravity data, Nevada Test Site, Nevada*, *U.S. Geol. Surv. Open-File Rept.*, 99-
681 310.
682 Poppeliers, C., and L. Preston (2019). The use of multiwavelets to quantify the uncertainty of
683 single-station surface wave dispersion estimates, *Seis. Res. Lett*. **90,** no. 2A, 754-764, doi:
684 10.1785/0220180145.
685 Preston, L.A. (2003). *Simultaneous Inversion of 3D Velocity Structure, Hypocenter Locations,*
686 *and Reflector Geometry in Cascadia*, Ph.D. Thesis, University of Washington Seattle, Seattle,
687 WA.
688 Preston, L., K. Smith, and D. von Seggern (2007). P-wave velocity structure in the Yucca
689 Mountain, Nevada, region, *J. Geophys. Res.* **112**, B11305, doi:10.1029/2007JB005005.
690 Preston, L. and D. von Seggern (2007). *Joint seismic tomography/location inversion in the*
691 *Reno/Carson City area: final report to the National Earthquake Hazard Reduction Program*,
692 USGS, Award Number 07HQGR0022,
693 http://earthquake.usgs.gov/research/external/reports/07HQGR0022.pdf.
694 Roecker, S., C. Ebinger, C. Tiberi, G. Mulibo, R. Ferdinand-Wambura, K. Mtelela, G. Kianji, A.
695 Muzuka, S. Gautier, J. Albaric, and S. Peyrat (2017), Subsurface images of the Eastern Rift,
696 Africa, from joint inversion of body waves, surface waves and gravity: investigating the role
697 of fluids in early-stage continental rifting, *Geophys. J. Int.* **210**, 931-950, doi:
698 10.1093/gji/ggx220.
699 Roecker, S., C. Thurber, and D. McPhee (2004), Joint inversion of gravity and arrival time data
700 from Parkfield: New constraints on structure and hypocenter locations near the SAFOD drill
701 site, *Geophys. Res. Lett.* **31**, L12S04, doi: 10.1029/2003GL019396.

Ruzek, B., J. Plomerova, and V. Babuska (2012). Joint inversion of teleseismic P waveforms and surface-wave group velocities from ambient noise in the Bohemian Massif, *Stud. Geophys. Geod.* **56**, 107-140, doi: 10.1007/s11200-010-9089-7.

Saltus, R.W., and G.A. Thompson (1995), Why is it downhill from Tonopah to Las Vegas?: A case for mantle plume support of the high northern Basin and Range, *Tectonics* **14** (6), 1235-1244.

Schramm, K.A., R.E. Abbott, M. Asten, S. Bilek, A. Pancha, H.J. Patton (2012), Broadband Rayleigh-Wave Dispersion Curve and Shear-Wave Velocity Structure for Yucca Flat, Nevada, *Bull. Seis. Soc. Am.* **102**, no. 4, 1361-1372, doi:10.1785/0120110296.

Shapiro, N.M., M. Campillo, L. Stehly, and M.H. Ritzwoller (2005). High resolution surface wave tomography from ambient seismic noise, *Science* **307**, 1615-1618.

Smith, K.D., L. Li, J.N. Brune, R. Anooshehpoor, and M.K. Savage (2000). *Preliminary results from the NPE-Ryan reversed refraction profile, in Geologic and Geophysical Characterization Studies of Yucca Mountain, Nevada, a Potential High-Level Radioactive-Waste Repository* [CD-ROM], edited by J.W. Whitney and W.R. Keefer, *Digital Data Ser. DDS-058*, 9, USGS, Denver, CO.

Snelson, C.M., R.E. Abbott, S.T. Broome, R.J. Mellors, H.J. Patton, A.J. Sussman, M.J. Townsend, and W.R. Walter (2013). Chemical Explosion Experiments to Improve Nuclear Test Monitoring, *EOS Trans.* **94**, no. 27, 237-239.

Springer, D.L., G.A. Pawloski, J.L. Ricca, R.F. Rohrer, and D.K. Smith (2002). Seismic source summary for all U.S. below-surface nuclear explosions, *Bull. Seis. Soc. Am.* **92,** no. 5, 1806-1840.

724 Stewart, J. H. (1988). Tectonics of the Walker Lane Belt, western Great Basin; Mesozoic and
725 Cenozoic deformation in a zone of shear, in *Metamorphism and Crustal Evolution of the*
726 *Western United States*, edited by W. G. Ernst, pp. 683–713, Prentice-Hall, Englewood Cliffs,
727 NJ.
728 Syracuse, E.M., H. Zhang, and M. Maceira (2017). Joint inversion of seismic and gravity data
729 for imaging seismic velocity structure of the crust and upper mantle beneath Utah, United
730 States, *Tectonophysics* **718**, 105-117, doi: 10.1016/j.tecto.2017.07.005.
731 Toney, L.D., R.E. Abbott, L.A. Preston, D.G. Tang, T. Finley-Hatton, and K.E. Phillips-Alonge
732 (2019). Joint body- and surface-wave tomography of Yucca Flat, NV using a novel seismic
733 source, *Bull. Seis. Soc. Am.* **109**, no. 5, 1922-1934, doi: 10.1785/0120180322.
734 Turcotte, D.L., and G. Schubert (1982). *Geodynamics*, John Wiley and Sons, New York, NY.
735 Vaniman, T. D., B. M. Crowe, and E. W. Gladney (1982). Petrology and geochemistry of
736 hawaiite lavas from Crater Flat, Nevada, *Contrib. Mineral Petrol*. **80**, no. 4, 341–357.
737 Vidale, J. (1990). Finite-difference calculation of traveltimes in three dimensions, *Geophysics*
738 ***55,*** no. 5, 521-526.
739 Waldhauser, F., and W.L. Ellsworth (2000). Double-difference earthquake location algorithm:
740 method and application to the Northern Hayward Fault, California, *Bull. Seis. Soc. Am.* **90**,
741 no. 6, 1353-1368.
742 Wapenaar, K., D. Draganov, R. Snieder, X. Campman, A. Verdel (2010). Tutorial on seismic
743 interferometry: Part 1- Basic principles and applications, *Geophysics* **75**, no. 5, 1SO-Z116,
744 doi: 10.1190/1.3457445.

Zhang, H., M. Maceira, P. Roux, and C. Thurber (2014). Joint inversion of body-wave arrival times and surface-wave dispersion for three-dimensional seismic structure around SAFOD, *Pure Appl. Geophys*. **171,** no. 11, 3013-3032, doi: 10.1007/s00024-014-0806-y.

Author Addresses:

Leiph Preston

Geophysics Department

P.O. Box 5800 MS-0750

Sandia National Laboratories

Albuquerque, New Mexico, USA

Christian Poppeliers

Geophysics Department

P.O. Box 5800 MS-0750

Sandia National Laboratories

Albuquerque, New Mexico, USA

David J. Schodt

Geophysics Department

P.O. Box 5800 MS-0750

Sandia National Laboratories

Albuquerque, New Mexico, USA.

Now at University of New Mexico, Albuquerque, NM.

Tables:

Table 1: Final weighted RMS (wRMS) and variance reduction (Var Red) relative to the starting 3-D model for various data types. The first 5 listed are body waves.

Data Type	**wRMS**	**Var Red (%)**
Earthquake P	0.06 s	74%*
Earthquake S	0.09 s	60%*
Active Source P	0.04 s	75%*
Differential P	7 ms	>99%†
Differential S	7 ms	>99%†
Gravity	5.32 mgal	99%
Group Speed	0.20 km/s	82%
Phase Speed	0.07 km/s	86%

* Only includes new data added to the Preston *et al.* (2007) data set. For S-waves from earthquakes this also includes S-waves added to existing events that only had P-picks in Preston *et al.* (2007).

† To nearest whole percentage, differential times variance reductions actually round to 100%, but are 99.5% and 99.7% variance reductions for P and S, respectively, to higher precision.

List of Figure Captions

Figure 1: Maps of study region with shaded relief. a) Geologic and geographic reference map: SCCC: Silent Canyon Caldera complex, PM: Pahute Mesa, RM: Rainier Mesa, SR: Syncline Ridge, TM: Timber Mountain, YF: Yucca Flat, CF: Crater Flat, YM: Yucca Mountain, JF: Jackass Flat, RVFZ: Rock Valley Fault Zone, FM: Funeral Mountains, AB: Amargosa Basin, DV: Death Valley, SPE: Source Physics Experiment site. Outline of NNSS and NV-CA state line indicated by black lines. b) Data summary map: Black dots are earthquakes; red symbols are active sources, including nuclear experiments; green triangles are seismic stations used in the study. Dashed cyan line shows cross-section for Figure 9. Outline of NNSS indicated by white line. Scale bars in km.

Figure 2: Station pairs used in the ambient noise cross-correlation study. Lower map is of the entire study region, while upper map shows the region enclosed in the rectangle. Scale bars in km.

Figure 3: Example of estimating group and phase speed using ambient noise. a) The cross correlogram for station pair NCF and GWY, filtered to a pass band of 1-10 seconds. b) The multiwavelet dispersion analysis, performed with ten wavelet pairs. The colormap shows the normalized wavelet transform for the first wavelet pair, where the small red crosses correspond to the peak wavelet amplitude for each period. The heavy black curve is the mean peak wavelet amplitude for all ten wavelet decompositions and corresponds to the mean dispersion curve estimate. The thin red curves correspond to plus/minus one standard deviation. c) The group-

and phase-speed estimated from the cross correlogram. The blue curve is simply the inverse of the mean dispersion curve from panel (b), along with plus/minus one standard deviation. The red curve is the computed phase speed, estimated by constructing a phase matched filter. d) The phase matched filter, when cross correlated with the original cross correlogram will form a zero-lag, symmetric wavelet for all frequencies. Note that in this example, the phase matched filter is unable to extract the phase speed for periods smaller than approximately 1.0 seconds.

Figure 4: Complete Bouguer gravity anomaly (CBA) data points used in the inversion. Scale bar in km.

Figure 5: Overlapping inversion grid layout. Black solid points represent the background Vp/Vs regular grid. Larger circles demark the grid points that comprise the irregular surface wave grid. The topographic surface is indicated by the curved line at top, and light filled circles are regular Vp/Vs grid nodes above the topographic surface. The Vp/Vs and surface wave grids exactly match each other from the topographic surface down to three nodes below the lowest topography. Below that depth, the surface wave grid coarsens by a factor of two for three surface wave nodes in depth, below which the surface wave grid coarsens again by a factor of two. This continues until the bottom of the model domain. The Vp grid spatially exactly matches the points of the Vp/Vs grid. The gravity grid behaves like the surface wave grid.

Figure 6: Comparison of body-wave-only tomography (a) and joint body wave, gravity, and surface wave inversion (b) at 0 km depth (sea level) for Vp. Black points are sources

826 (earthquake and active) within 1 km of the depth section. The estimated P-wave velocity is
827 shown as a color map draped over shaded relief. Scale bars in km.
828
829 **Figure 7: Comparison of Vs checkerboards from a) P- and S-body-wave and gravity**
830 **tomography and b) joint body wave, gravity, and surface wave inversion at 37.2°N. Vs**
831 **checkerboard with ±10% perturbation with 20 km horizontal by 4 km vertical blocks**.
832
833 **Figure 8**: P-wave velocity depth-sections at depths of a) -1 km (or 1km above sea level) b) 1
834 km, c) 2 km, d) 4 km, e) 10 km, and f) 15 km. P-wave velocity is indicated by the color bars and
835 are only shown where body or surface wave data exist. The estimated velocities are draped over
836 the shaded relief map. The small black dots indicate the locations of earthquakes. See S1-S6 for
837 expanded versions of panels.
838
839 **Figure 9**: Vp cross-section at 37°N (cyan dashed line in Figure 1b) from the surface to 15 km
840 depth. Black points are earthquakes, active sources, or gravity measurement points within 0.05°
841 of the cross-section. Approximate locations for GP: Grapevine Peak, BH: Bullfrog Hills, OV:
842 Oasis Valley, TM: Timber Mountain, BM: Buckboard Mesa, ER: Eleana Range, YF: Yucca Flat.
843
844 **Figure 10**: Vp/Vs depth sections at depths of a)-1 km, b) 1 km, c) 2 km, d) 4 km, e) 10 km, and
845 f) 15 km. Colored only where body wave or surface wave data exist. The small black dots
846 indicate the locations of earthquakes. Dashed lines in e) and f) denote the approximate southern
847 limit of resolvability based on 40 km x 40 km checkerboards (see Figure 12d). See S7-S12 for
848 expanded versions of these panels.

849

850 **Figure 11**: Checkerboard tests for Vp estimated by the joint inversion for various depths and
851 block sizes. a) 6km x 6km block size at a depth of 0km, b) 10km x 10km block size at a depth of
852 0km, c) 10km x 10km block size at a depth of 4km, d) 20km x 20km block size at a depth of
853 0km, e) 20km x 20km block size at a depth of 6km, and f) 40km x 40km block size at a depth of
854 10km. The black dots indicate the location of earthquakes.

855

856 Figure 12: Similar to Figure 11, but for Vp/Vs. a) 10km x 10km block size at a depth of 4km, b)
857 20km x 20km block size at a depth of 0km, c) 20km x 20km block size at a depth of 6km, and d)
858 40km x 40km block size at a depth of 10km. The black dots indicate the location of earthquakes.

859

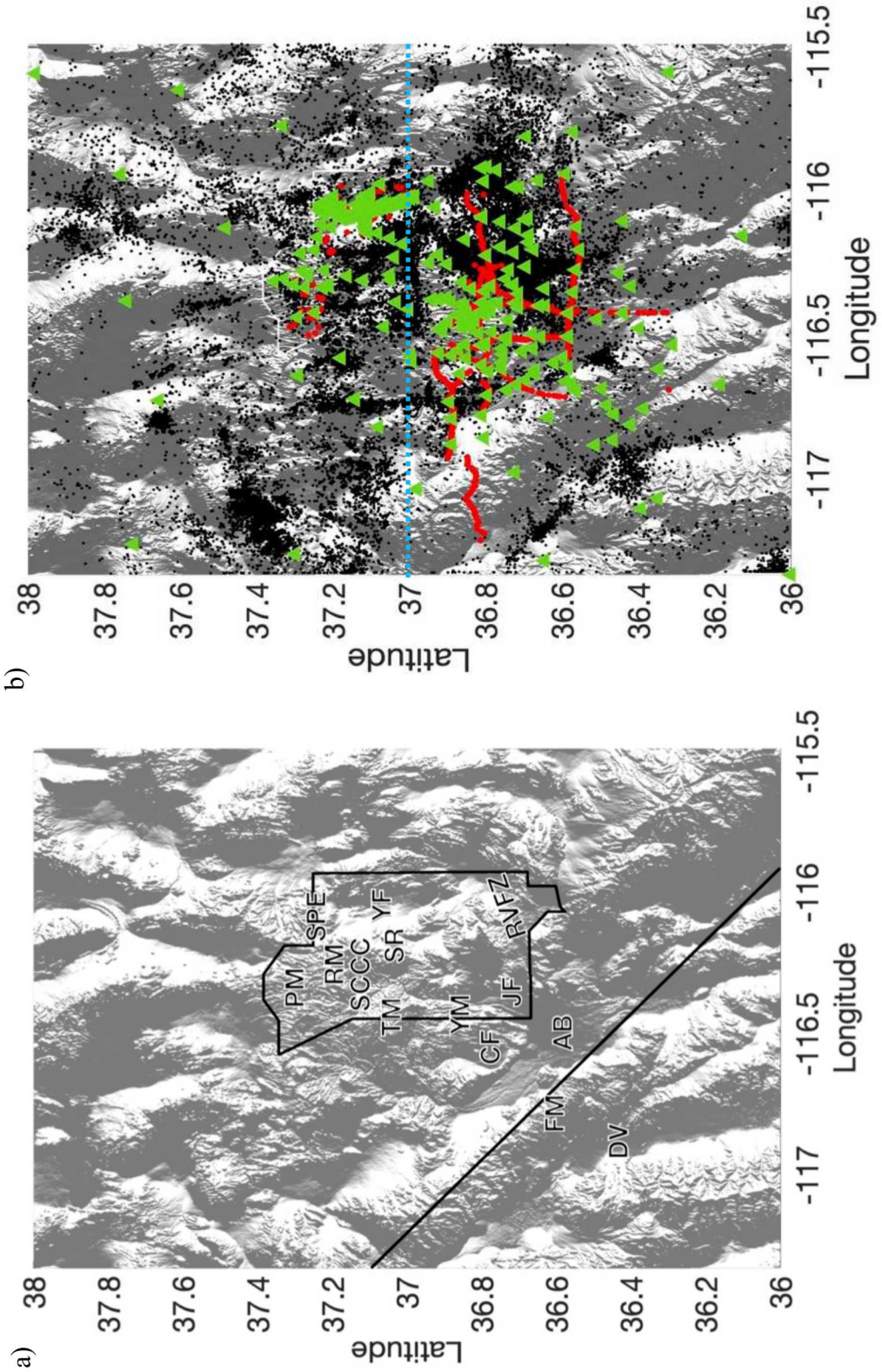

860 **Figure 1**:

861 Maps of study region with shaded relief. a) Geologic and geographic reference map: SCCC:

Silent Canyon Caldera complex, PM: Pahute Mesa, RM: Rainier Mesa, SR: Syncline Ridge, TM: Timber Mountain, YF: Yucca Flat, CF: Crater Flat, YM: Yucca Mountain, JF: Jackass Flat, RVFZ: Rock Valley Fault Zone, FM: Funeral Mountains, AB: Amargosa Basin, DV: Death Valley, SPE: Source Physics Experiment site. Outline of NNSS and NV-CA state line indicated by black lines. b) Data summary map: Black dots are earthquakes; red symbols are active sources, including nuclear tests; green triangles are seismic stations used in the study. Dashed cyan line shows cross-section for Figure 9. Outline of NNSS indicated by white line.

871

872 Figure 2:

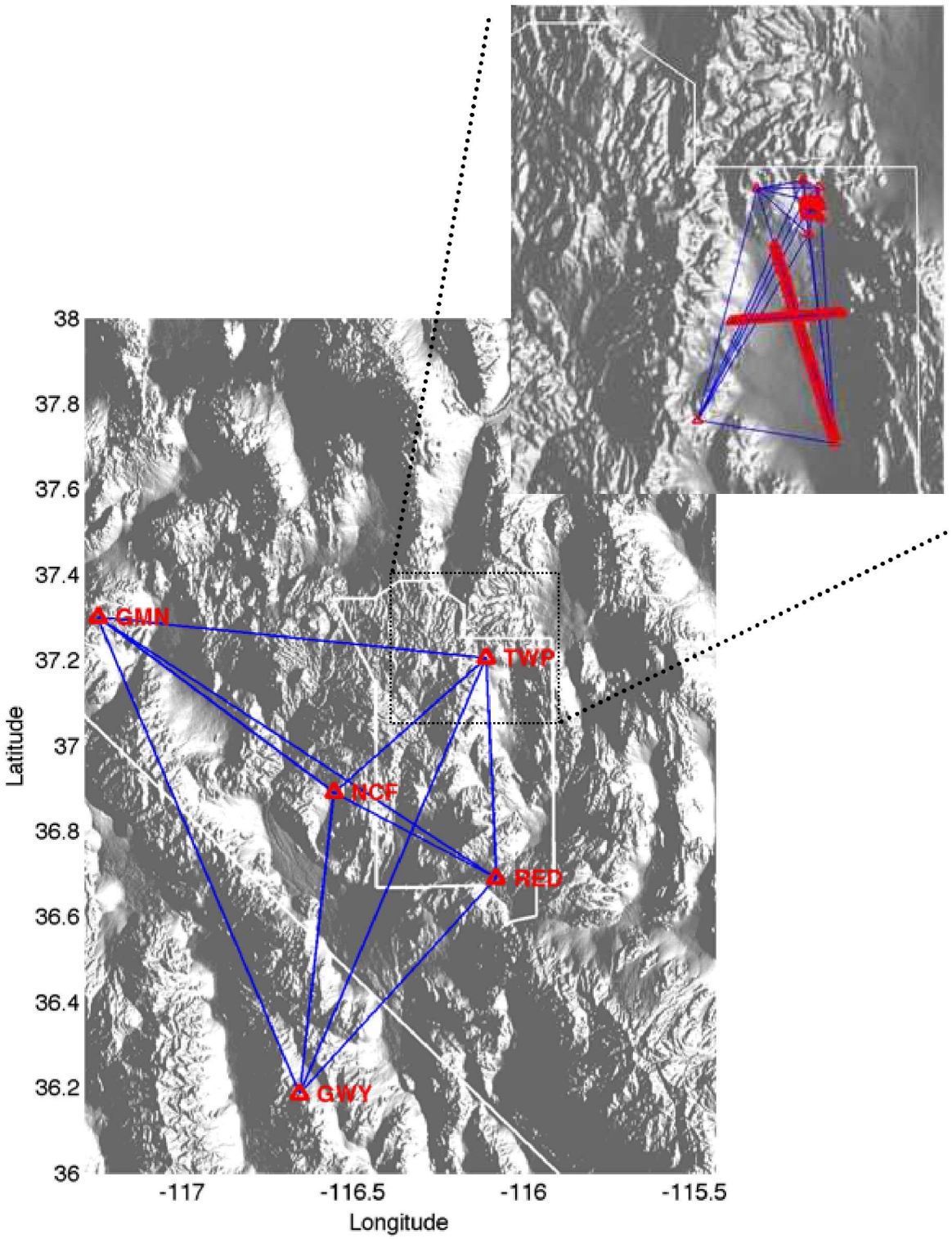

873

874 **Figure 2**: Station pairs used in the ambient noise cross-correlation study. Lower map is of the
875 entire study region, while upper map shows the region enclosed in the rectangle.
876

Figure 3:

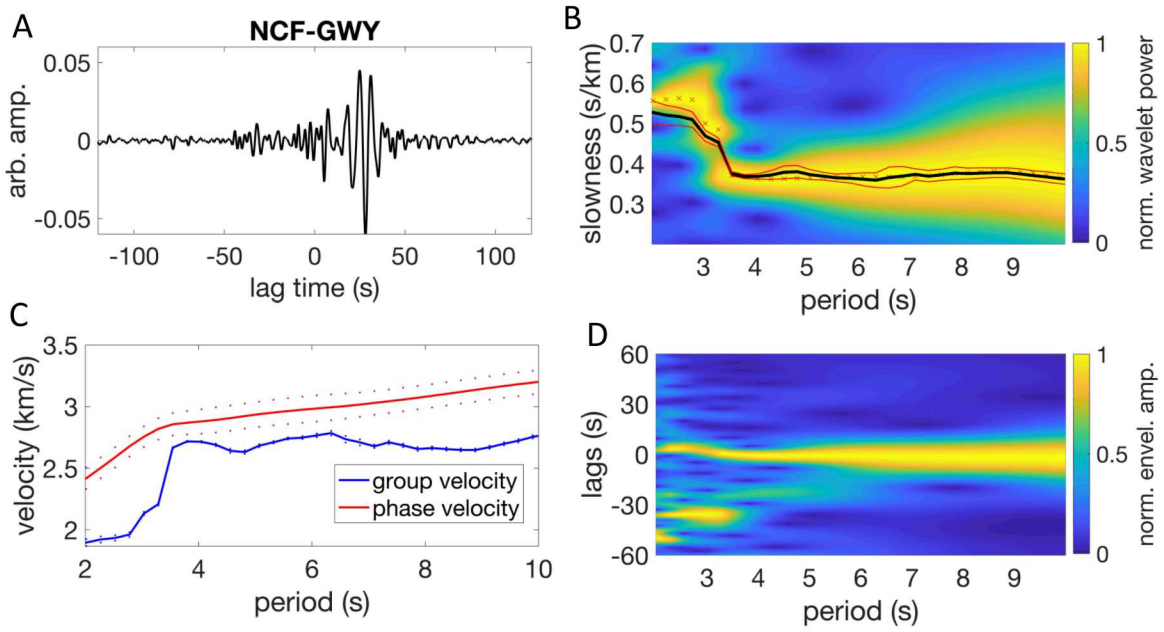

Figure 3: Example of estimating group and phase speed using ambient noise. a) The cross correlogram for station pair NCF and GWY, filtered to a pass band of 1-16 seconds. b) The multiwavelet dispersion analysis was performed with ten wavelet pairs. The colormap shows the normalized wavelet transform for the first wavelet pair, where the small red crosses correspond to the peak wavelet amplitude for each period. The heavy black curve is the mean peak wavelet amplitude for all ten wavelet decompositions and corresponds to the mean dispersion curve estimate. The thin red curves correspond to plus/minus one standard deviation. c) The group- and phase-speed estimated from the cross correlogram. The blue curve is simply the inverse of the mean dispersion curve from panel (b), along with plus/minus one standard deviation. The red curve is the computed phase speed, estimated by constructing a phase matched filter. d) The phase matched filter, when cross correlated with the original cross correlogram will form a zero-lag, symmetric wavelet for all frequencies. Note that in this example, the phase matched filter is unable to extract the phase speed for periods smaller than approximately 1.0 seconds.

892

893

894 Figure 4:

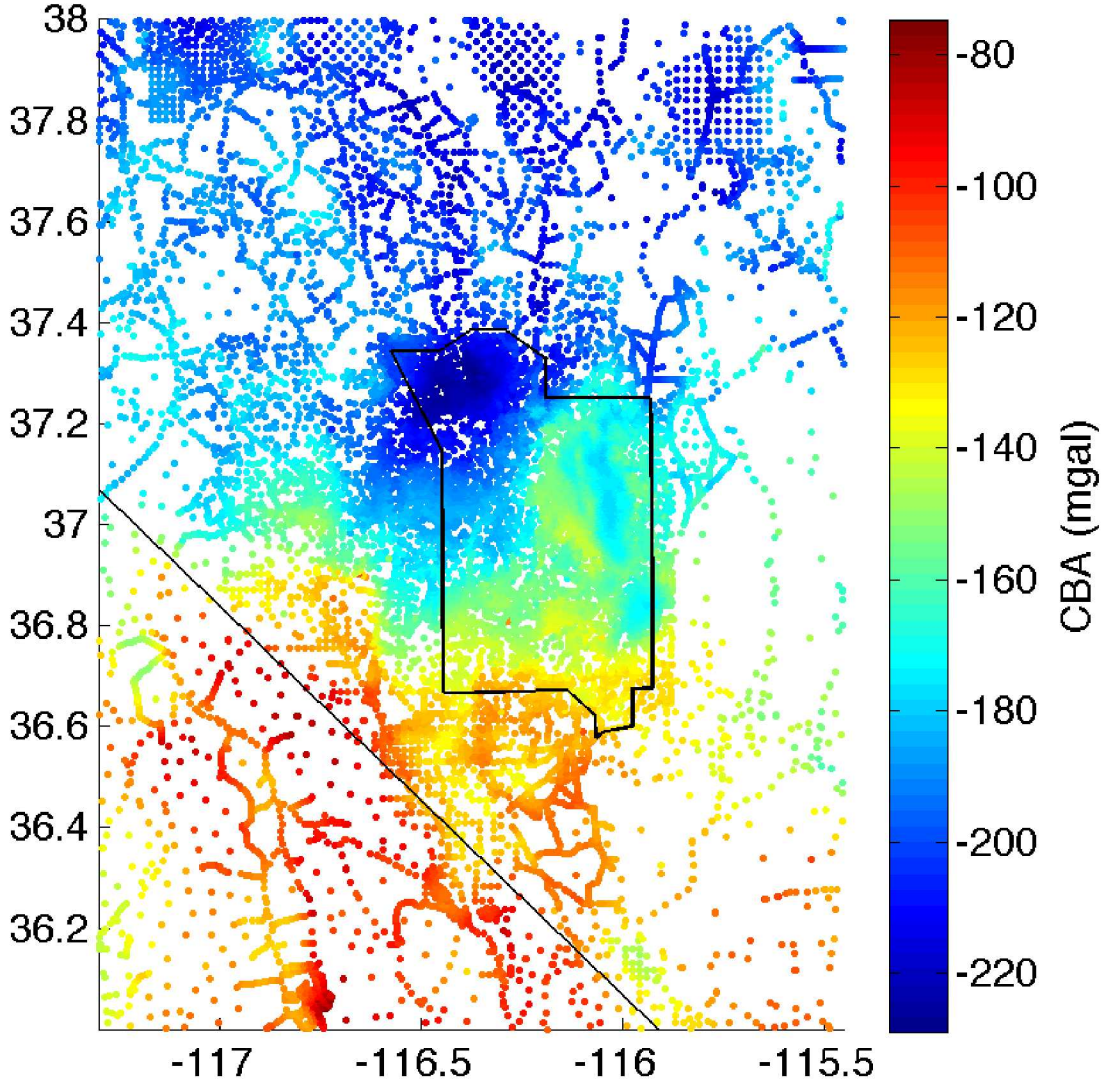

895
896 **Figure 4**: Complete Bouguer gravity anomaly (CBA) data points used in the inversion.

897
898
899
900

Figure 5

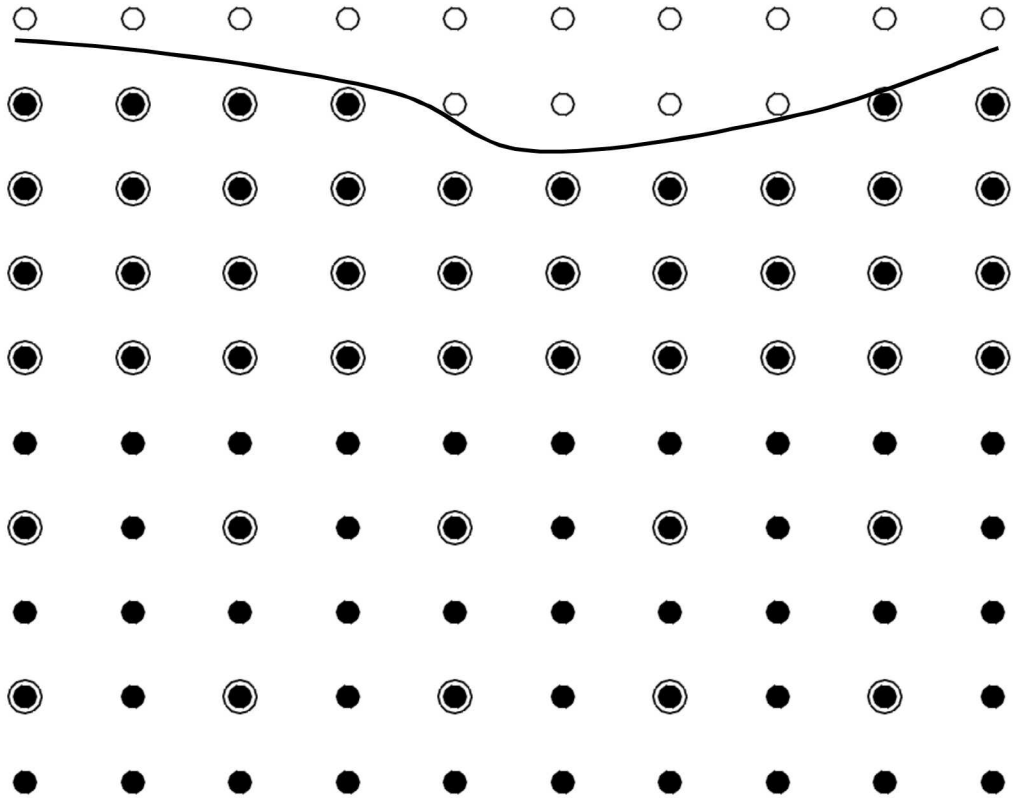

Figure 5: Overlapping inversion grid layout. Black solid points represent the background Vp/Vs regular grid. Larger circles demark the grid points that comprise the irregular surface wave grid. The topographic surface is indicated by the curved line at top, and light filled circles are regular Vp/Vs grid nodes above the topographic surface. The Vp/Vs and surface wave grids exactly match each other from the topographic surface down to three nodes below the lowest topography. Below that depth, the surface wave grid coarsens by a factor of two for three surface wave nodes in depth, below which the surface wave grid coarsens again by a factor of two. This continues until the bottom of the model domain. The Vp grid spatially exactly matches the points of the Vp/Vs grid. The gravity grid behaves like the surface wave grid.

913

914

915

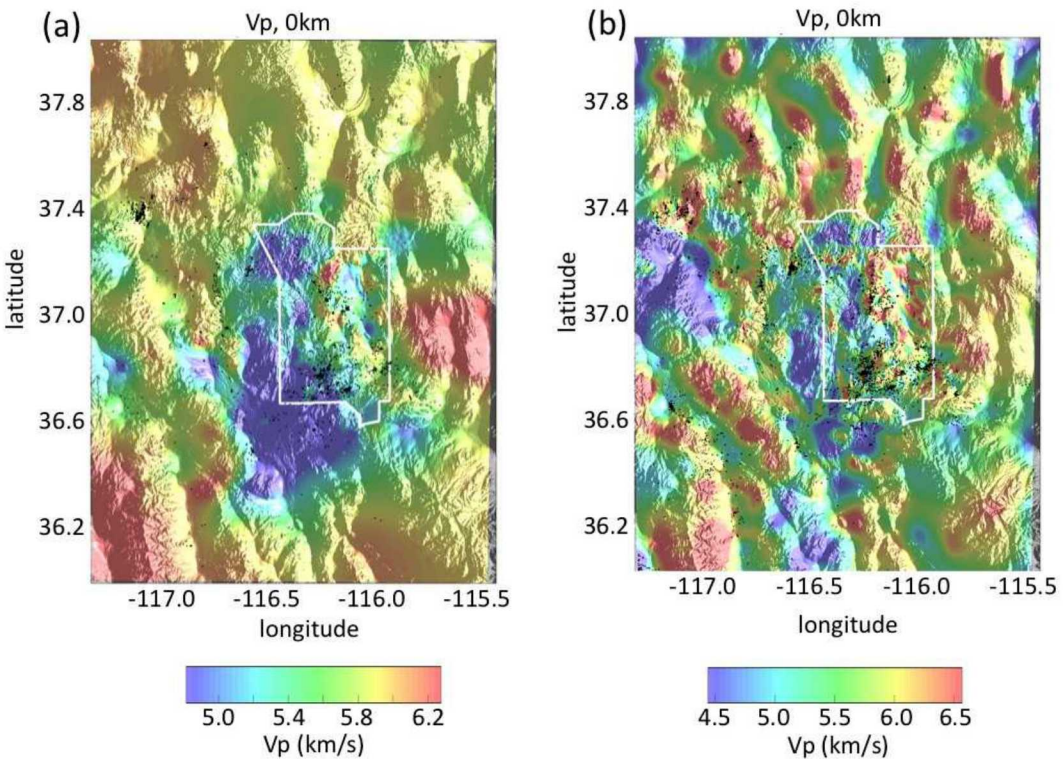

916

917 **Figure 6**: Comparison of body-wave-only tomography (a) and joint body wave, gravity, and
918 surface wave inversion (b) at 0 km depth (sea level) for Vp. Black points are sources
919 (earthquake and active) within 1 km of the depth section. The estimated P-wave velocity is
920 shown as a color map draped over shaded relief.

921

922

a)

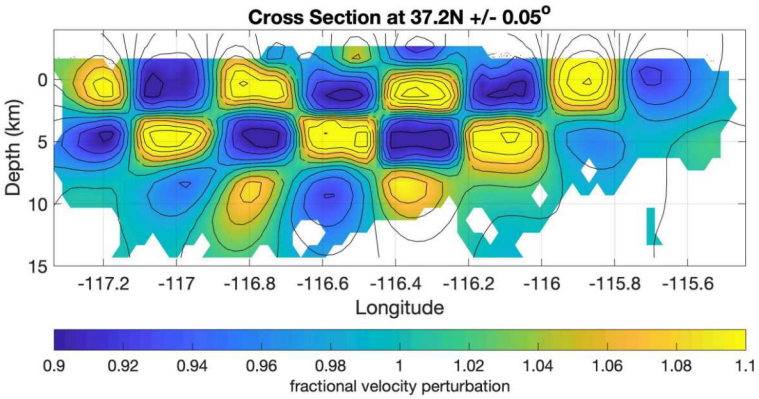

923

b)

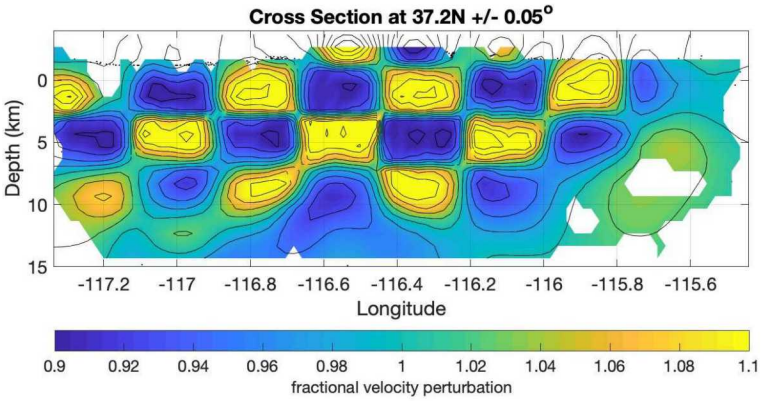

924

925 **Figure 7**: Comparison of Vs checkerboards from a) P- and S-body-wave and gravity tomography

926 and b) joint body wave, gravity, and surface wave inversion at 37.2°N km. Vs checkerboard

927 with ±10% perturbation with 20 km horizontal by 4 km vertical blocks.

928

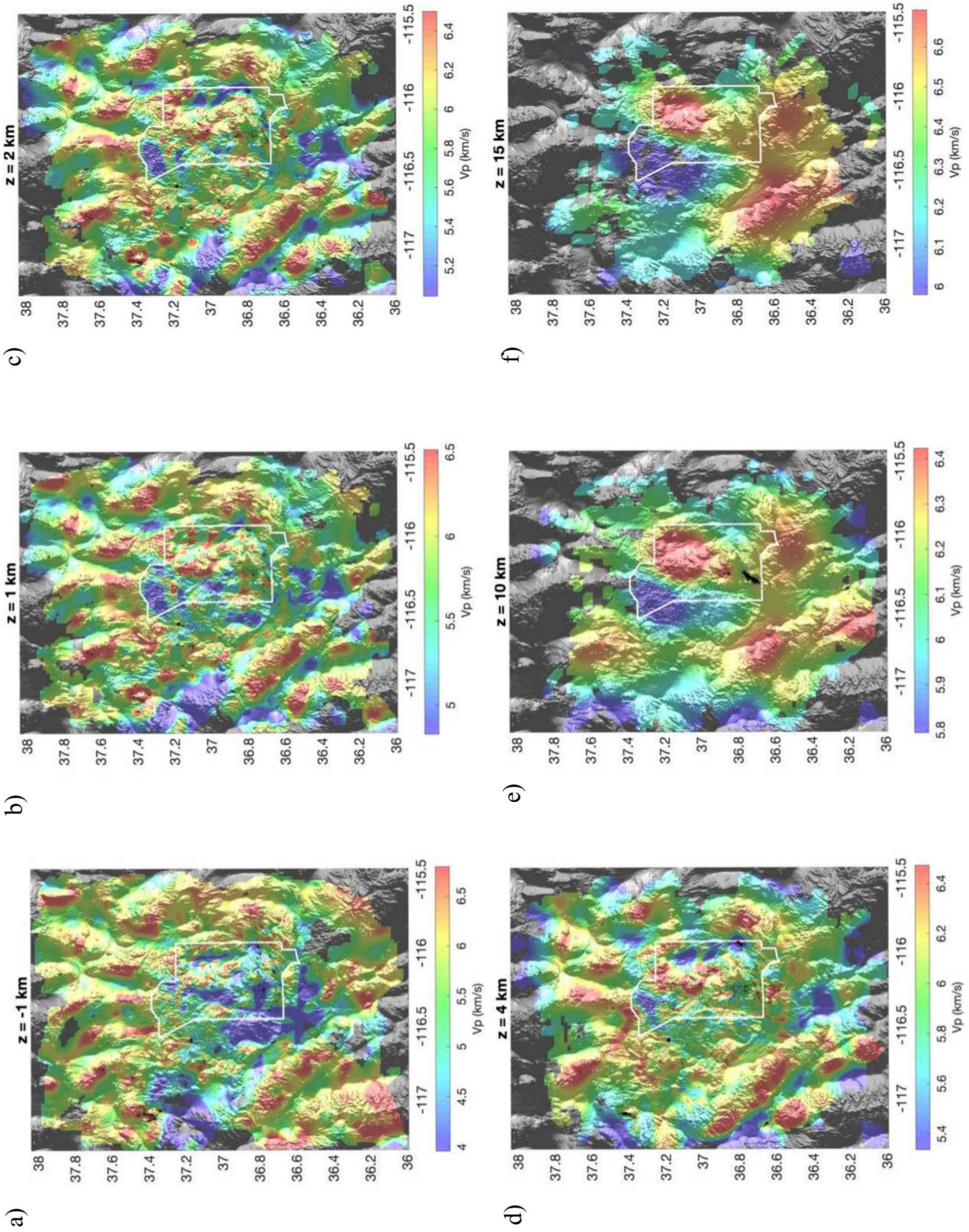

929

930 **Figure 8**: P-wave velocity depth-sections at depths of a) -1 km (or 1km above sea level) b) 1

km, c) 2km, d) 4km, e) 10km, and f) 15km. P-wave velocity is indicated by the color bars and are only shown where body or surface wave data exist. The estimated velocities are draped over the shaded relief map. The small black dots indicate the locations of earthquakes. See S1-S6 for expanded versions of panels.

936

937 Figure 9:

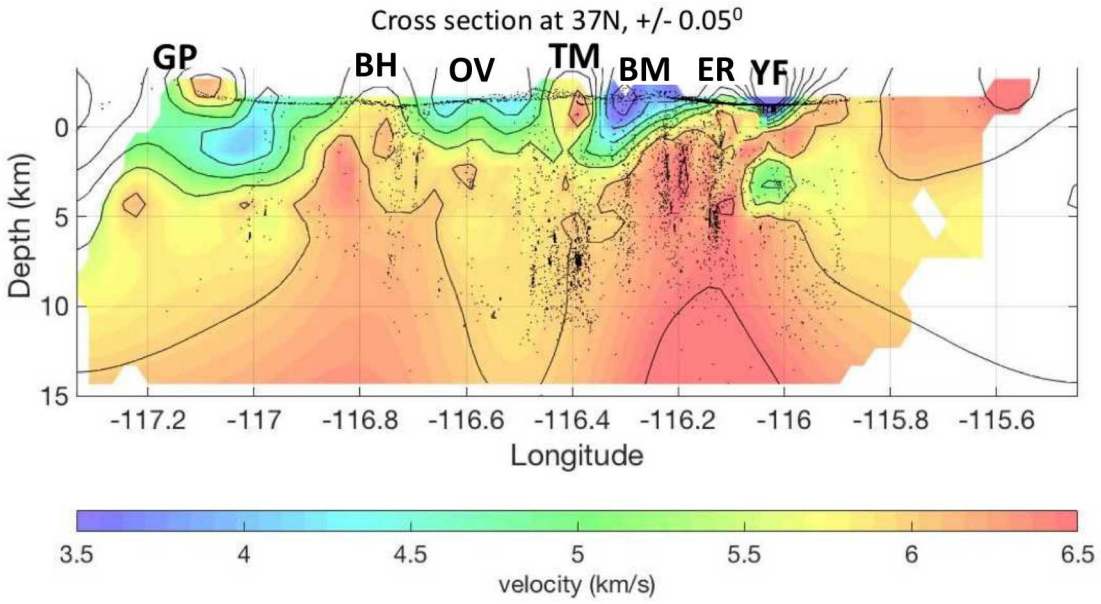

938

939 **Figure 9**: Vp cross-section at 37°N (cyan dashed line in Figure 1a) from the surface to 15 km

940 depth. Black points are earthquakes, active sources, or gravity measurement points within 0.05°

941 of the cross-section. Approximate locations for GP: Grapevine Peak, BH: Bullfrog Hills, OV:

942 Oasis Valley, TM: Timber Mountain, BM: Buckboard Mesa, ER: Eleana Range, YF: Yucca Flat.

943

944

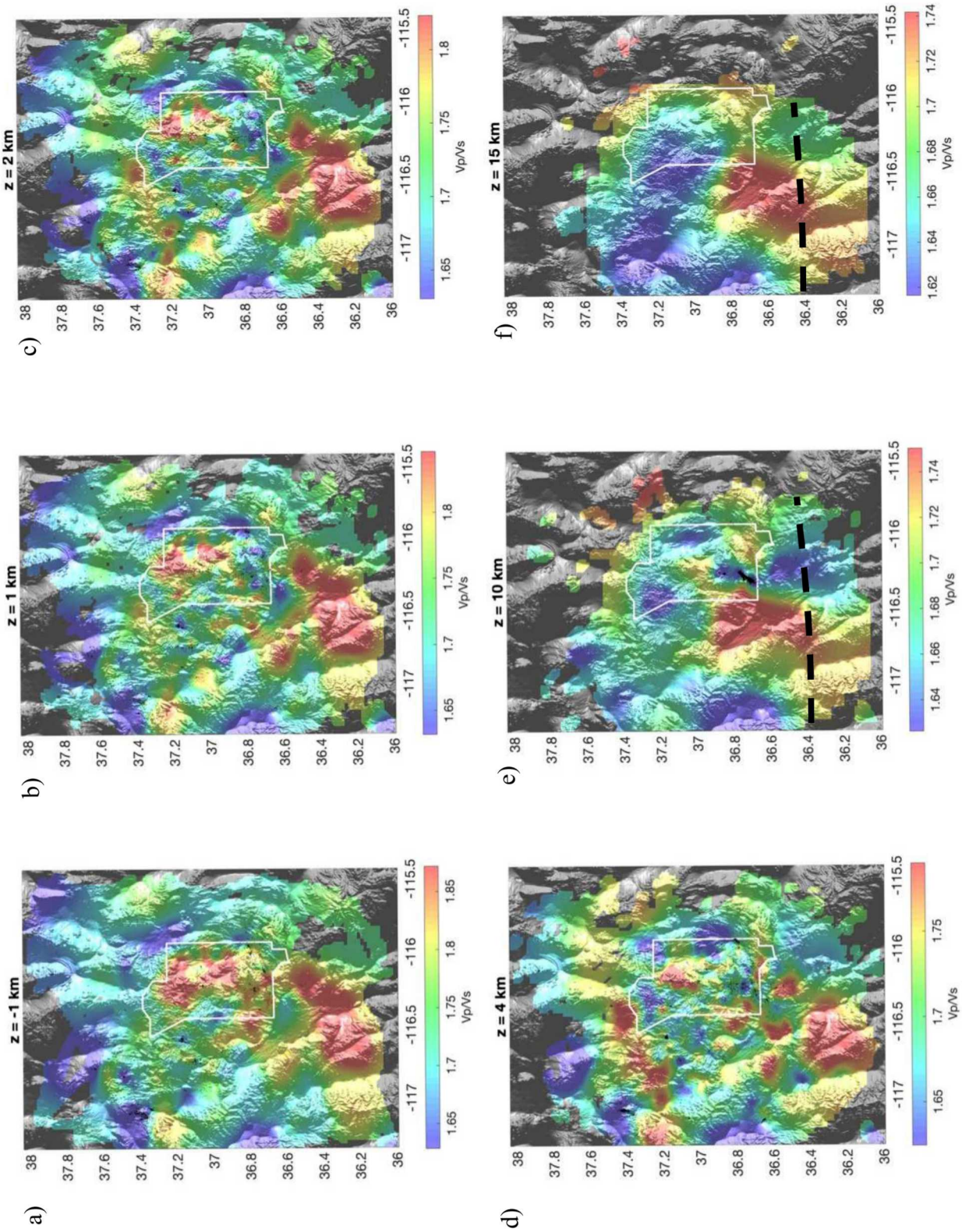

945

946 **Figure 10**: Vp/Vs depth sections at depths of a)-1km, b) 1km, c) 2km, d) 4km, e) 10km, and f)

15km. Colored only where body wave or surface wave data exist. The small black dots indicate the locations of earthquakes. Dashed lines in e) and f) denote the approximate southern limit of resolvability based on 40 km x 40 km checkerboards (see Figure 12d). See S7-S12 for expanded versions of these panels.

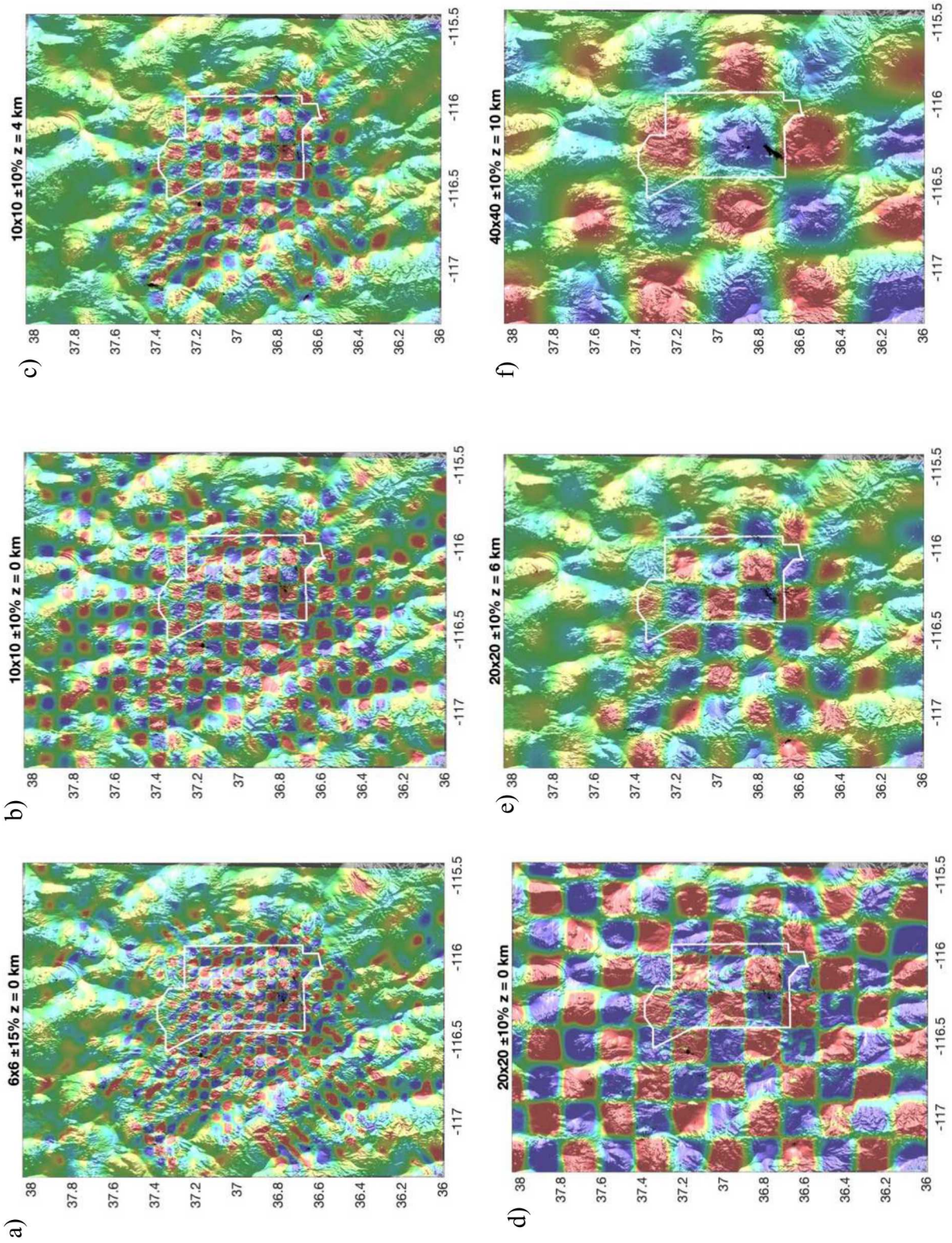

952

953 **Figure 11**: Checkerboard tests for Vp estimated by the joint inversion for various depths and

954 block sizes. a) 6km x 6km block size at a depth of 0km, b) 10km x 10km block size at a depth of

955 0km, c) 10km x 10km block size at a depth of 4km, d) 20km x 20km block size at a depth of

956 0km, e) 20km x 20km block size at a depth of 6km, and f) 40km x 40km block size at a depth of

957 10km. The black dots indicate the location of earthquakes.

958

959

960 Figure 12:

961

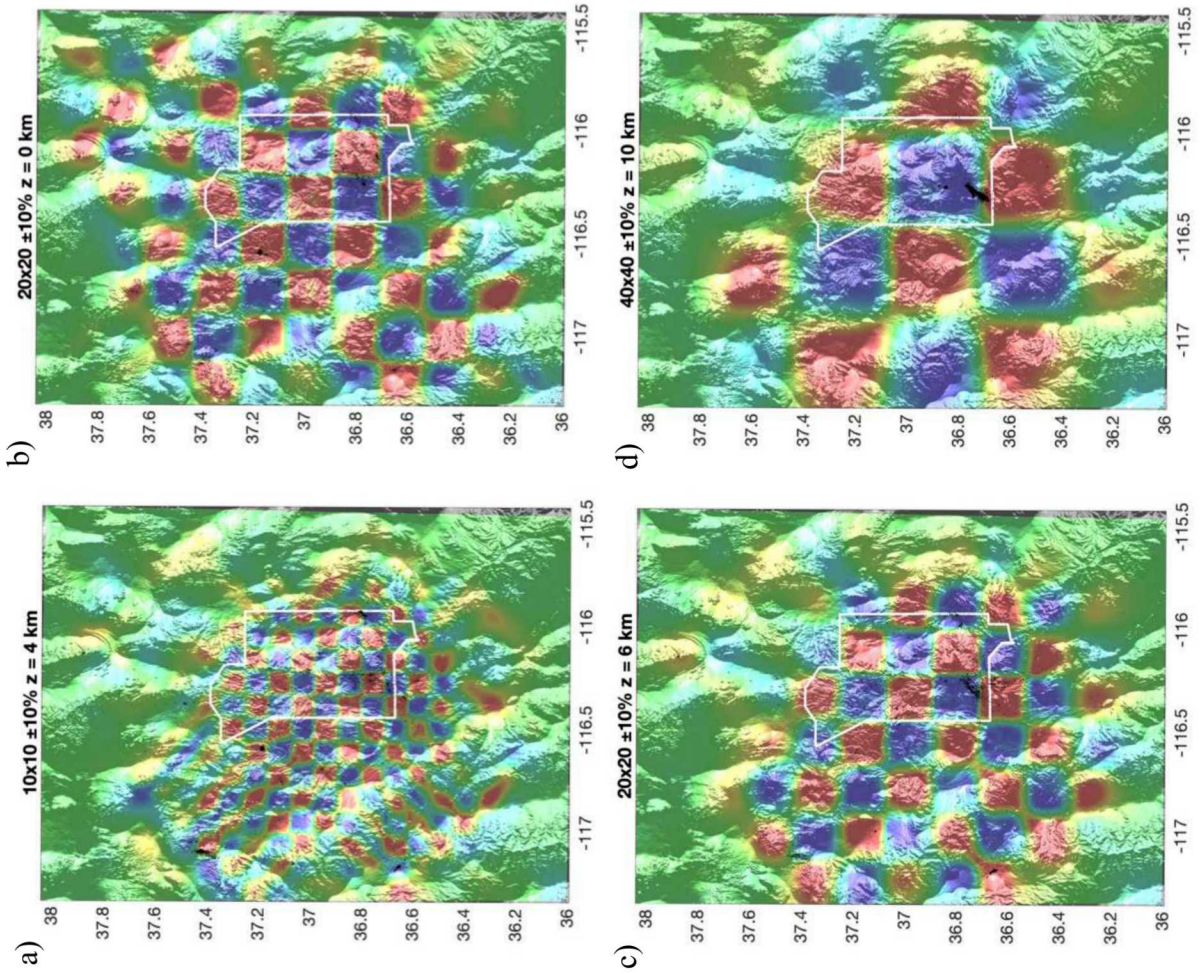

962

963 Figure 12: Similar to Figure 11, but for Vp/Vs. a) 10km x 10km block size at a depth of 4km, b)

964 20km x 20km block size at a depth of 0km, c) 20km x 20km block size at a depth of 6km, and d)

965 40km x 40km block size at a depth of 10km. The black dots indicate the location of earthquakes.

966

967